



Supercritical melt flow in high-speed laser welding and its interdependence with the geometry of the keyhole and the melt pool

Eveline N. Reinheimer¹ · Peter Berger¹ · Christian Hagenlocher¹ · Rudolf Weber¹ · Thomas Graf¹

Received: 8 August 2023 / Accepted: 14 February 2024 / Published online: 23 February 2024
© The Author(s) 2024

Abstract

The advent of undercuts and humping limits the applicable speed of deep-penetration laser welding. Recent findings additionally show that a significant change of the keyhole's shape is associated with the occurrence of undercuts. Considering that undercuts and humping are melt flow-induced defects, this leads to the question of how the geometry of the keyhole and the melt pool influence the melt flow and vice versa. In this work, the Froude number was used to characterize the melt flow around a keyhole. X-ray images of the keyhole and cross-sections of the weld were therefore used to determine the geometrical boundaries of the melt flow, to estimate the average melt velocity around the keyhole, and finally determine its Froude number. The flow around a cylindrically shaped keyhole was found to always be subcritical, whereas supercritical melt flow was observed around the elongated keyholes that are formed at higher welding speed. The findings may be interpreted in the sense that the elongation of the keyhole is a consequence of a supercritical stream of the melt flowing underneath and around the keyhole. This perception is consistent with the long-known experience that humping may be avoided by reducing the flow speed of the melt by widening the melt pool surrounding the keyhole (e.g., by means of beam shaping) and suggest a new explanation for the elongation of the keyhole at increased welding speed.

Keywords High-speed laser welding · Melt flow · Keyhole · Supercritical flow · Froude number

1 Introduction

With the currently available high-power lasers, high feed rates of more than 0.3 m/s can be realized in deep-penetration laser welding of metal parts with welding depths exceeding 1.5 mm. Beyond a high process efficiency [1], high-speed laser welding of metals has the further benefits of a stable keyhole [2] and the avoidance of depth fluctuations and pores [3]. High welding velocities are required especially for parts with long weld seams, e.g., cooling plates of battery cases in electro mobility [4]. However, when the welding velocity is too high, undercuts and humping [5–7] occur, marking the upper limit of the process window. Since more than 45 years, humping and undercuts have been reported for different welding processes. After it was first observed in gas metal arc welding (GMAW) [8], it was also found to occur in other welding processes [9, 10] such as

gas tungsten arc welding (GTAW) [11, 12], electron beam welding [13–15], and laser beam welding [7, 16–18]. All the reported studies identified different influencing factors, including but not exclusively the ambient atmosphere, surface condition, metal composition, and heat input. It also has been observed that the melt flow in the weld pool significantly impacts the advent of these defects. Especially in laser welding, the vapor keyhole and the melt flow surrounding this keyhole have been identified to have a strong impact on the occurrence of humping and undercuts at high welding velocities [19–22]. Previous works [7, 23–25] showed that the keyhole's geometry elongates backwards with increasing welding velocity and that this is associated with the occurrence of undercuts and humping.

The instability of a fast liquid jet was described by Anno et al. [26]. Albright et al. [27] later interpreted the occurrence of humping as a consequence of a jet instability of the melt flow. Shimada [28] suggested in 1983 that a supercritical flow must be present to cause humping, which was subsequently reaffirmed by Ngyuen [29] in 2005. The phenomenon of supercritical flow is well-known in open channel flows and is characterized by a flow velocity u that exceeds

✉ Eveline N. Reinheimer
Eveline-nicole.reinheimer@ifsw.uni-stuttgart.de

¹ University of Stuttgart (IFSW), Pfaffenwaldring 43,
70569 Stuttgart, Germany

the propagation velocity $c = \sqrt{gy}$ of a surface wave, where y is the characteristic depth of the liquid and g is the acceleration of gravity [30]. The Froude number [31]

$$Fr = \frac{u}{\sqrt{gy}}, \quad (1)$$

is used to characterize a melt flow to be subcritical ($Fr < 1$), critical ($Fr = 1$), or supercritical ($Fr > 1$). The Froude number can also be considered the ratio between the inertia force and gravity force in the flow. If $Fr < 1$, the buoyancy or gravity force dominates the liquid flow [32–34]. When the threshold of $Fr = 1$ is exceeded, the flow abruptly transits to the supercritical condition with a characteristic hydraulic jump further downstream, where the flow has slowed down enough to again become subcritical [35].

Uddin's study [36] already emphasizes that the Froude number serves as a suitable parameter for characterizing flow conditions in laser beam welding. In his research, the welding depth was used as the characteristic depth y , and he successfully correlated the occurrence of humping with Froude numbers larger than 1. Harroni et al. [37] also adopted the Froude number (using the length of the weld pool as the characteristic length y) to assess the quality of the weld surface and to relate the occurrence of humping to supercritical conditions with $Fr > 1$.

The association between undercuts, humping, and the sudden transformation of the keyhole's geometry, as described in [24, 38], leads to the hypothesis that supercritical flows within the weld pool exert an influence on the keyhole's geometry at elevated welding speeds. The aim of this work is therefore to consider this hypothesis by examining the Froude criterion for a wide set of parameters in laser beam welding. The 3D geometries of the keyhole, which were reconstructed from X-ray images and cross-sections of the weld were used to determine the velocity of the melt flow at the narrowest position in the channel given by the geometry of the melt pool and the obstruction of the keyhole. The results reveal a direct relation between the geometry of the keyhole and the Froude number of the melt flow at the narrowest position in the channel. By considering the distribution of the Froude number alongside the differently shaped keyholes it was found that a subcritical flow is clearly present all-around cylindrical keyholes, while a supercritical flow is present in the region immediately behind the front of elongated (U-shaped and wedge-shaped) keyholes up to their trailing end, where the flow becomes subcritical again. The novelty of this work consists in the experimental method to determine the velocity of the melt flow around the vapor keyhole and the characterization of the melt flow induced by laser welding using the Froude number. The novel finding of this work is that a supercritical flow is clearly present when the keyhole exhibits a U or a wedged shape and that this fast

melt flow influences the rear wall of the keyhole when laser welding with high feed rates. Additionally, it was shown that beam shaping is a useful method to adjust the Froude number of the melt flow around the keyhole. It was shown that an adjustment of the Froude number along the keyhole influences the shape of the keyhole resulting in the avoidance of undercuts at high welding speeds.

2 Determination of the Froude number in the melt flow

For the following discussion, we consider the melt flow in the channel which is formed by the geometry of the weld pool and the obstruction of the keyhole as sketched in Fig. 1. The origin of the coordinate system is chosen to be located at the front of the keyhole's opening on the surface of the workpiece. An average value $\bar{u}(x)$ of the flow velocity of the melt (averaged over the cross-section of the flow channel) can be calculated at any position x along the welding direction by considering the volume flow rate \dot{V} of the melt in the channel. The cross-sectional area $A_{ch}(x) = A_S - A_C(x)$ of the flow channel is given by

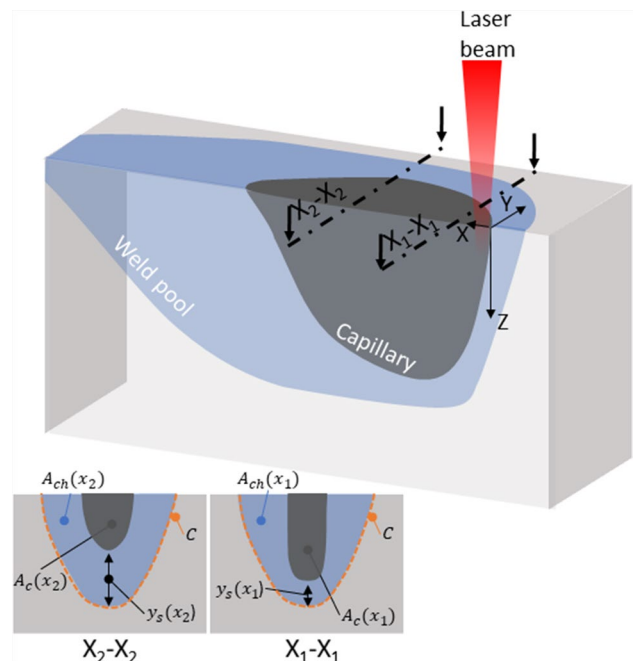


Fig. 1 Sketch of the geometry of the keyhole (grey), the weld pool (blue), and the used coordinate system with its origin at the front of the keyhole at the surface of the workpiece. The cross-sectional area $A_{ch}(x)$ of the flow channel (light blue) and the transverse cross-sectional area $A_c(x)$ of the vapor keyhole (dark grey) are shown for two different x -positions. For the present study, the outer contour of the melt pool, the wetted circumference C (orange dashed line), was extracted from cross-sections of welded seams and the 3D shape of the keyhole was reconstructed from x-ray images

the difference between the cross-sectional area A_S of the weld pool and the transverse cross-sectional area $A_C(x)$ of the keyhole (red). For the sake of simplicity, it is assumed that A_S is approximately constant in the region at the side of the keyhole and is simply given by the cross-sectional area of the weld seam. In the inertial reference system of the welded workpiece in which the keyhole moves with the welding speed v , the average flow velocity of the incompressible melt follows from the conservation of mass and is then given by

$$\bar{u}(x) = \frac{\dot{V}}{A_{ch}(x)} - v = \frac{\dot{V}}{A_S - A_C(x)} - v, \tag{2}$$

where the volume rate of the melt flow around the keyhole amounts to

$$\dot{V} = A_S \cdot v \tag{3}$$

The latter is a good approximation at positions alongside the keyhole where the weld pool has its largest width and where the volume flow \dot{V} of the melt is therefore virtually not changed by additional melting or solidification. As we have no suitable means to measure the transverse distribution of the flow velocity in the cross-section of the flow channel around the keyhole, the following discussion is limited to the average values defined and used in (1) to (3). It is obvious from (2) that the highest average melt velocity prevails at the location where the channel of the melt flow has its smallest cross-section.

In the case of laser beam welding, the characteristic depth y of the melt flow is determined by the outer dimensions of the weld pool and the keyhole. As the cross section of the flow is not rectangular, the depth y used in Eq. (1) may either be defined by the quotient

$$y_C = \frac{A_{ch}}{C}, \tag{4}$$

of the cross-sectional area A_{ch} of the flow channel and the wetted circumference C [39], cf. Figure 1, or alternatively directly by the depth

$$y_s = s - s_c \tag{5}$$

of the melt below the keyhole, where s is the welding depth and s_c is the depth of the keyhole. We will see below that the main findings do not depend on which of the two characteristic depths are used. Inserting Eq. (4) for y and Eq. (2) for u into (1) yields

$$Fr_c = \frac{\frac{\dot{V}}{A_S - A_C(x)} - v}{\sqrt{g \frac{A_{ch}}{C}}}. \tag{6}$$

Using Eq. (5) instead of (4) on the other hand leads to

$$Fr_s = \frac{\frac{\dot{V}}{A_S - A_C(x)} - v}{\sqrt{g(s - s_c)}}. \tag{7}$$

3 Experimental

A disk laser (TruDisk 16,002, Trumpf) with a wavelength of 1.03 μm and a maximum cw power of 16 kW was used for the experiments that were conducted with different sets of parameters. The welding speed v ranged between 0.07 and 0.92 $\text{m} \cdot \text{s}^{-1}$. All experiments were performed on aluminum EN-AW6082. Different beam delivery fibers and different focusing lenses were used to obtain various diameters d_f of the beam waist. A collimation with a focal length of 200 mm was used for all experiments. The used combinations of the beam delivery fibers and focusing lenses are shown in Table 1 together with the resulting diameters of the beam waists and the used welding parameters for each beam diameter.

The beam waist was positioned on the surface of the samples and had a top-hat intensity profile for all experiments. The laser power was adjusted to keep the welding depth s between 1 and 2.5 mm. The samples were clamped on a linear axis which moved them beneath a stationary processing optics. A table with all relevant experimental parameters can be found in Appendix.

In order to calculate the average flow velocity using Eq. (2), we have determined A_S from cross-sections of the welded seams. The areas $A_C(x)$ were extracted from the 3D shape of the keyhole which was reconstructed from x-ray images. The x-ray imaging system used to determine the shape of the keyhole by radiographing the processing zone in the transvers y -direction is described in detail in [40–43]. An x-ray tube FXE-224.48 by Comet Yxlon with a minimum spot size of 6 μm , and an acceleration voltage of 60 kV with a current of 1.4 mA was used. A scintillator by Hamamatsu, Shizuoka, Japan, with 728 \times 728 pixels with a resulting resolution of 58 pixel \cdot mm $^{-1}$ was used to convert the x-rays in visible light which was recorded with high-speed camera SA5 by Photron. Typical time-averaged x-ray images recorded by this system are shown in row (a) of Fig. 2 for three typical keyhole geometries. The contour of the keyhole is highlighted by the dash-dotted lines. The depth of the melt pool corresponds to the welding depth seen in the cross sections of the welds in row (c) and is based on the assumption that the melt pool reaches its full depth already at $x = d_f/2$ and that no solidification of the melt takes place in the region near the keyhole. The length of the time-averaged keyhole at the sample's surface and the depth of the keyhole are referred to as l_c and s_c , respectively, in the following. Exploiting the information of the attenuation

Table 1 Overview of used beam delivery fibers and focusing lenses with the resulting diameters of the beam waist and the used welding speeds and laser power

Core diameter d_c of beam delivery fiber in μm	Focal length f_f of focusing lens in mm	Diameter d_f of beam waist in μm	Welding speed v in $\text{m} \cdot \text{s}^{-1}$	Laser power in kW
200	200	200	0.07	1.525
			0.13	1.65
400	250	500	0.13	5
			0.33	10
			0.5	10
			0.07	3.25
400	315	630	0.5	16
			0.6	16
			0.92	16
			0.4	12
200	680	680	0.5	16
			0.67	16
			0.27	16
			0.3	16
400	500	1000	0.37	14
			0.37	16
			0.53	16
			0.13	11
400	680	1360	0.2	16

of the x-ray radiation contained in the grey values of the recorded images, the transverse width and hence the 3D shape of the keyhole can be derived using Beer's law [43, 44], cf. row (b) in Fig. 2. For the present study, the keyhole is categorized as a cylindrical vapor keyhole when the length of the keyhole l_c approximately equals the beam diameter d_f . The keyhole is referred to as U-shaped when $1 \lesssim l_c \leq 4d_f$ and as a wedge-shaped keyhole when $l_c > 4d_f$. The surfaces of the corresponding weld seams are shown in row (d). The width of the weld seam on the surface is indicated with b .

4 Results

The average melt velocity $\bar{u}(x)$ given by Eq. (2) and the resulting Froude numbers were determined for the three characteristic keyholes listed in Fig. 2. The data points shown in the figures following below represent the average value of three measurements while the error bars correspond to the standard deviation of the three measurements. The top left graph in Fig. 3 shows the distribution of the average flow velocity $\bar{u}(x)$ along the time-averaged cylindrical keyhole. The top middle graph in Fig. 3 shows the distribution of the average flow velocity $\bar{u}(x)$ along the time-averaged U-shaped keyhole, and the one on the top right shows the distribution of the average flow velocity $\bar{u}(x)$ along the time-averaged wedge-shaped keyhole. Starting from $x = d_f/2$, the flow velocity is seen to first increase (due to an increased

width of the obstructing keyholes) with a following decrease for all three observed keyhole geometries. The cylindrical keyhole obtained at low welding speeds leads to the lowest average melt velocity. With the U-shaped keyhole, the flow velocity is seen to first increase until the position at $x = 0.9\text{mm}$ and then decrease again slightly from the position $x = 1.3\text{mm}$ up to $x = 2.2\text{mm}$. A similar observation is made with the wedge-shaped keyhole where the flow speed increases between the front of the keyhole and the position at $x = 1.3\text{mm}$, behind which it decreases again. In both latter cases, the flow speed reaches approximately the same maximum value, but the flow velocity decreases much faster in the case of the U-shaped keyhole.

The determined average melt velocities were used to calculate the respective Froude number, as shown in the lower part of Fig. 3 for the cylindrical (left), U-shaped (middle), and wedge-shaped (right) keyholes. As mentioned above, the two different characteristic lengths y_c , as given by Eq. (4), and y_s , as described in Eq. (6), were employed to determine the Froude numbers Fr_c (filled data points in Fig. 3) and Fr_s (empty data points in Fig. 3), respectively. For the cylindrical keyhole and the U-shaped keyhole, there is no significant difference between the two Froude numbers. No matter which definition of the characteristic depth y is used, the flow around the cylindrically shaped keyhole is found to always be subcritical. For the U-shaped keyhole, the flow is found to be supercritical near the keyhole's front, which may explain the elongation of the keyhole in comparison to

Fig. 2 Time-averaged x-ray image (a) and 3D reconstructions of the keyholes (b), cross-section of the weld seam (c), corresponding surface of the seam (d), and corresponding parameters (e) resulting in three typical keyhole geometries. The contours of the keyholes and the seam are highlighted by the dashed and dash-dotted lines, respectively

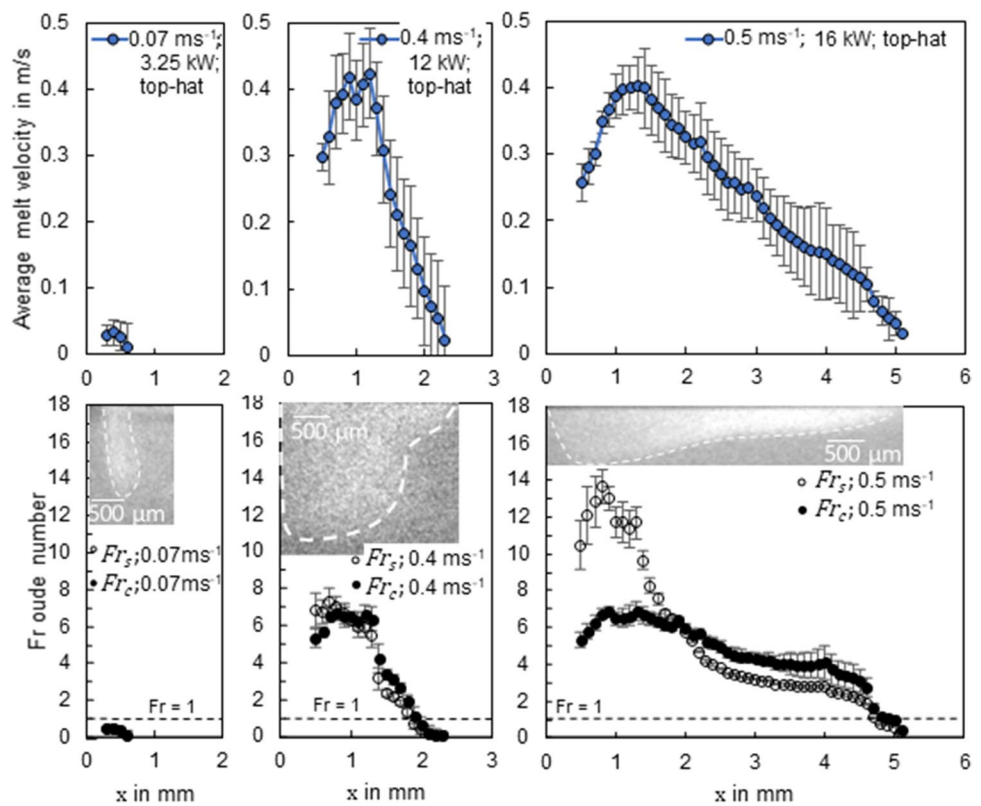
	Cylindrical keyhole	U-shaped keyhole	Wedge-shaped keyhole
(a) Time-averaged x-ray image of keyhole			
(b) 3D-Reconstruction			
(c) Cross-section			
(d) Weld surface			
(e) Weld parameters	$P = 3.25 \text{ kW};$ $v = 0.07 \text{ ms}^{-1};$ $d_f = 630 \text{ μm};$ $s = 2.43 \text{ mm};$ $b = 2.6 \text{ mm};$ $A_s = 4.07 \text{ mm}^2;$ $l_c = 0.67 \text{ mm};$ $s_c = 2 \text{ mm}$	$P = 12 \text{ kW};$ $v = 0.3 \text{ ms}^{-1};$ $d_f = 680 \text{ μm};$ $s = 1.75 \text{ mm};$ $b = 1.8 \text{ mm};$ $A_s = 2.07 \text{ mm}^2;$ $l_c = 2.3 \text{ mm};$ $s_c = 1.48 \text{ mm}$	$P = 16 \text{ kW};$ $v = 0.5 \text{ ms}^{-1};$ $d_f = 680 \text{ μm};$ $s = 1.4 \text{ mm};$ $b = 1.6 \text{ mm};$ $A_s = 1.78 \text{ mm}^2;$ $l_c = 5.1 \text{ mm};$ $s_c = 1.3 \text{ mm}$

the cylindrical vapor keyhole. Due to the fast decrease of the flow speed around the U-shaped keyhole, the flow returns to a subcritical condition for positions $x > 1.9\text{mm}$. The rear wall of the keyhole may be interpreted as the hydraulic jump at the transition from the supercritical to the subcritical flow condition. In the case of the wedge-shaped keyhole, the two different definitions of the characteristic depth y_c and y_s lead to a more pronounced difference in the resulting values of the Froude numbers, but the transitions between the supercritical to the subcritical flow conditions are found to occur approximately at the same location $x \approx 4.9\text{mm}$ and coincide approximately with the rear end of the keyhole. As the depth of the wedge-shaped keyhole decreases more significantly than its width between $x = 2$ and $x = 4.9$, Fr_s drops below Fr_c in this range. Near the end and behind the keyhole, the difference between the values of two characteristic depths defined in Eqs. (4) and (6) diminishes, also resulting in a smaller difference between the two Fr numbers. In the front section around the wedge-shaped keyhole, the difference between the values of the Froude numbers resulting from the two differently defined characteristic lengths y_s and y_c

could be an indication that the melt flow exhibits a higher Froude number below the keyhole compared to the flow at the side of the keyhole. Further back along the wedge-shaped keyhole, there is a significant decrease of its depth s_c , resulting in an increased value of y_s and therefore a decrease of Fr_s . Conversely, y_c and therefore Fr_c experiences only a small change. Towards the trailing end of the keyhole, both Froude numbers converge to similar values, suggesting an equalization of the flow conditions beneath and at the side of the keyhole. Further and more involved research will be needed to verify this preliminary interpretation.

As in the case of the U-shaped keyhole, the melt flow is again found to clearly be supercritical right from the front of the wedge-shaped keyhole. The significantly elongated keyhole may be interpreted to be a consequence of the high Froude numbers obtained for the melt flowing underneath the keyhole as characterized by the characteristic depth y_s and the correspondingly high Froude number Fr_s , where the inertia force dominates the melt flow. These findings confirm the existence of the fast liquid jet as described in the literature [26, 27] and show that this jet is not only

Fig. 3 Average flow speed $\bar{u}(x)$ according to Eq. (2) (top) and the resulting Froude numbers (bottom) in the melt pool around the keyhole for the time-averaged cylindrical, U-shaped, and wedge-shaped keyhole from Fig. 2



responsible for the formation of humping and undercuts but that especially the fast flow underneath the keyhole presumably also shapes the rear part of the keyhole at high welding speeds, as the supercritical melt flow which is dominated by the inertia force leads to a backward movement of the rear wall of the keyhole. Additionally, the wedge-shaped keyhole has previously been related to the presence of undercuts [25], which suggests that the fast jet may at least partly also be responsible for the formation of undercuts.

To further investigate the generality of the above findings, the Froude numbers were determined for a wide range of additional experimental parameters. The complete table with all experimental parameters and measured results is given in Appendix. Figure 4 shows the maximum averaged velocity $\bar{u}_{\max} = \max(\bar{u}(x))$ of the flow around the keyhole as determined for each set of parameters. Again, the lowest flow speed is found to occur in the case of the cylindrically shaped keyholes (blue). The average velocity of the flow around the U-shaped keyhole (green) is significantly higher, while the highest flow velocities are observed together with the wedge-shaped keyhole (orange). Apart from the fact that a U-shaped keyhole is formed at lower welding speeds, the latter is mainly due to the fact that the velocity of the melt rises with increased

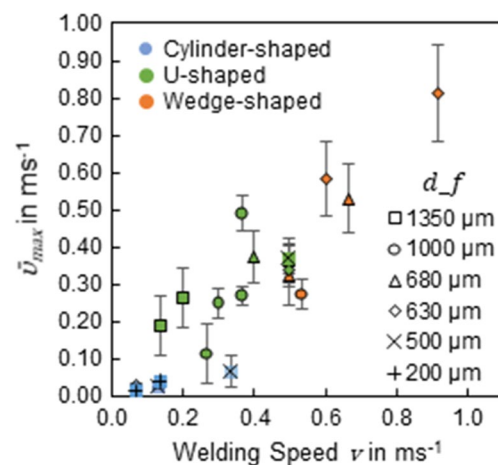


Fig. 4 Maximum average flow speed \bar{u}_{\max} according to Eq. (2) for welding speeds ranging from 0.07 to 0.83 ms⁻¹

welding speeds, as the channel surrounding the keyhole, through which the melt flows, becomes narrower with a simultaneous increase of the melt flow \dot{V} . Note that this finding applies regardless of the applied beam diameters.

The Froude number that corresponds to the determined values of \bar{u}_{\max} is shown in Fig. 5. No matter which definition of the characteristic depth y is used, the Froude

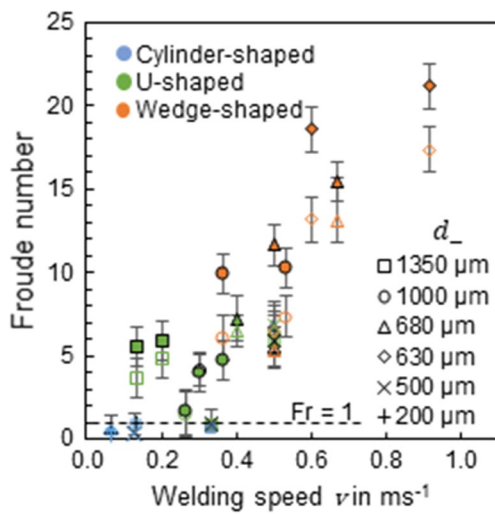
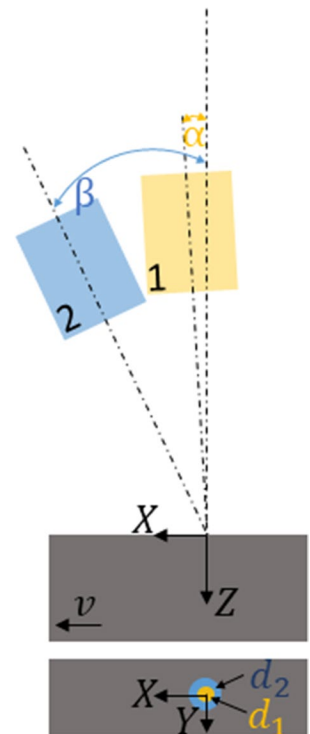


Fig. 5 Froude numbers Fr_s (filled symbols) and Fr_c (empty symbols) at the position with the highest average speed of the melt flow for welding speeds from 0.07 to 0.83 ms^{-1}

number is found to increase with increasing welding speed. For all cylindrically shaped keyholes (blue), the Froude numbers are < 1 and the corresponding flows hence subcritical. The Froude number exceeds the value of 1 for U-shaped keyholes (green) and increases to values beyond 5.5 for the wedge-shaped keyholes (orange). The correlation between the flow condition in the melt channel around the keyhole and the transition of the keyhole geometry form a cylindrical to a U-shaped and then to a wedge-shaped keyhole with increasing Froude number which is quite evident. The results suggest that the elongation of the keyhole first to a U shape and finally to a wedge shape is caused by a supercritical flow in the melt pool.

The shape of small cylindrical keyholes formed during welding at very low speeds is commonly considered to be a consequence of the balance of forces (e.g., evaporation pressure, surface tension, static pressure) on the keyhole’s wall [45]. This explanation reaches its limits at high welding speeds, when no significant radiation reaches the trailing end of the increasingly elongated keyhole. The presented results suggest that with increasing welding velocity and Froude numbers, the shape of the keyhole is influenced more by the hydrodynamics in the melt flow than by processes in the keyhole itself. Further developed experimental methods to determine the transverse distribution of the melt velocity across the flow channel will

Fig. 6 Arrangement of the two beams for welding with a graded intensity profile. Processing head 1 (orange) was inclined by $\alpha = 7^\circ$, processing head 2 (blue) was inclined by $\beta = 17^\circ$



be required in future research to investigate the impact of the melt flow on the shape of the keyhole in more details.

Based on this finding it can be concluded that in order to avoid supercritical flows and the resulting fast jet that causes undercuts and humping, the melt channel in the front region of the keyhole, where the highest melt velocity occurs, must be widened to obtain a reduced value of the Froude number.

5 Implication on the process

Based on this finding, one may conclude on the advantage of beam shaping which is a well-known method to avoid humping and undercuts in laser beam welding [46–49] by widening the weld pool around the keyhole and hence reduce the flow speed in the melt.

This relation is discussed in the following at the example of an experiment in which the intensity distribution was shaped using a setup with two processing heads to geometrically superimpose the beams from two separate lasers on the surface of the welded sample [23]. The axes of both beams were positioned to intersect on the sample’s surface as sketched in Fig. 6. The TruDisk16002 laser with the same beam delivery fiber with a core diameter of 200 μm as described above was used for one beam (processing head 1

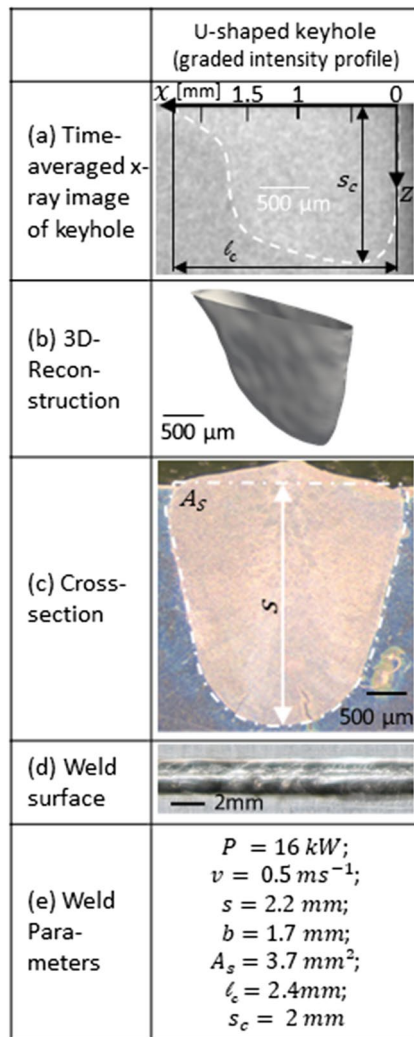


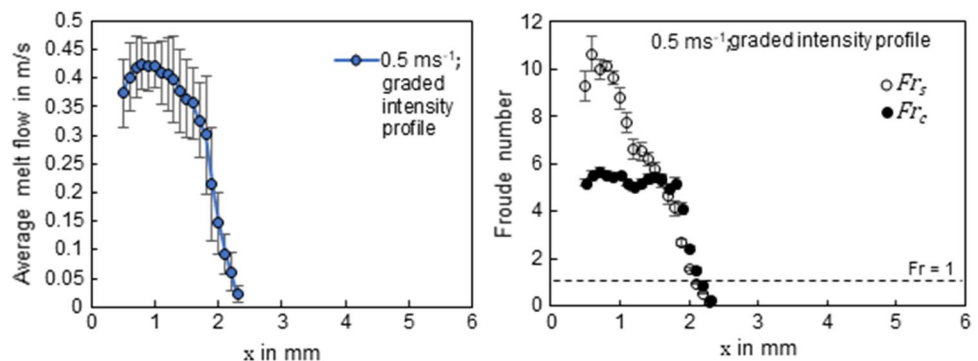
Fig. 7 Time-averaged x-ray image of the keyhole (a), the resulting 3D reconstruction of the keyhole (b), cross-section of the weld seam which was used to determine the size of the weld pool (c), the resulting weld surface (d), and the operating parameters (e) for the keyhole resulting from a graduated intensity profile

in Fig. 6). Using a collimation with a focal length of 200 mm and a focusing lens with a focal length of 560 mm resulted in a diameter of the beam waist of $d_{f1} = 560 \mu\text{m}$ with a top-hat intensity profile. The waist of this beam was again positioned on the surface of the welded sample. The second laser was a TruDisk8001 with a beam delivery fiber with a core diameter of 200 μm . Using a collimation with a focal length of 200 mm and a focusing lens with a focal length of 560 mm resulted in a diameter of the beam waist of $d_{f2} = 560 \mu\text{m}$ with a top-hat intensity profile and a Rayleigh length of $z_R = 7.84 \text{ mm}$. The waist of this second beam (processing head 2 in Fig. 6) was positioned at 5 mm above the sample, resulting in a beam diameter of $d_2 = 660 \mu\text{m}$ on the surface of the sample with a more Gaussian-like intensity distribution. This method to shape the intensity profile on the sample's surface was chosen because it was easy to implement at the multi-kW power level. Other approaches may be used in the future for further investigations. The resulting graded intensity distribution corresponds to the superposition of a top-hat and a Gaussian intensity profile with the abovementioned diameters of 560 μm and 660 μm , respectively. The advantage of this intensity profile is that the highest intensity is positioned in the center and decreases continuously towards the outside. Both lasers were operated with the same power of 8 kW each.

A typical time-averaged x-ray image recorded using the above-described system is shown in row (a) of Fig. 7 for a weld with the graded intensity profile. The contour of the keyhole is highlighted by the dash-dotted line. The depth of the melt pool corresponds to the welding depth seen in the cross-sections of the welds in row (c). The length of the time-averaged keyhole at the sample's surface l_c and the depth of the keyhole are indicated in row (a). The reconstructed geometry of the time-averaged keyhole is shown in row (b).

When the graded intensity distribution with a total power of 16 kW was used at the welding speed of $0.5 \text{ m} \cdot \text{s}^{-1}$, the keyhole was found to again exhibit a similar

Fig. 8 Average flow speed $\bar{u}(x)$ according to Eq. (2) (left) and the resulting Froude numbers $Fr(x)$ in the melt pool (right) around the keyhole for the time-averaged U-shaped keyhole formed during welding with a graded intensity profile



U-shape as in the case of the top-hat-shaped beam at a speed of $0.4 \text{ m} \cdot \text{s}^{-1}$, cf. Figures 2 and 7, and the seam shows no undercuts. Figure 8 (left) shows the distribution of the average flow velocity $\bar{u}(x)$ along the time-averaged keyhole from Fig. 7 that was obtained with the graded intensity distribution. As it was described above for the welds obtained with a top-hat intensity distribution, it was seen that starting from $x = d_t/2$, the flow velocity increases due to an increasing width of the obstructing keyhole with a following decrease.

The corresponding Froude numbers are shown in the Fig. 8 (right) either using Eq. (6) (filled datapoints) or Eq. (7) (empty data points). It is striking that up to the position $x = 1.7\text{mm}$, the distribution is similar to the one shown in Fig. 3 (bottom right) for the wedge-shaped keyhole welded at the same welding speed with a top-hat intensity distribution but with a pronounced difference in the absolute values of the Froude numbers. For all positions $x > 1.7\text{mm}$, the distribution is similar to the one of the U-shaped keyhole welded at a lower welding speed with a top-hat intensity distribution, and the difference between Fr_s and Fr_C vanishes; both Froude numbers decrease to a subcritical flow within a short distance.

The results again show that there is a fast melt jet near the leading front of the keyhole, as it is seen for the wedge-shaped keyhole from Fig. 2 at the same welding speed. Probably due to the widening of the weld pool around the keyhole, this fast jet is slowed down quite rapidly for positions $x > 1.7\text{mm}$ and decreases to a subcritical flow at the position $x = 2.2\text{mm}$. The Froude numbers obtained with Eq. 7 for the flow below the keyhole in the weld performed with the graded intensity distribution is generally lower than the ones obtained for the wedge-shaped keyhole at the same welding speed. The steep decrease to a subcritical flow seen when welding with the graded intensity distribution presumably prevents a further elongation of the keyhole resulting in a U-shaped keyhole at the same welding speed for which a wedge-shaped keyhole was obtained with a top-hat intensity profile. Furthermore, the results reinforce the assumption

that the occurrence of undercuts is related with critical flow conditions at an elongated keyhole, since no undercuts occurred at the weld with the graded intensity profile.

6 Conclusion

Considering the Froude number of the melt flow around a keyhole reveals a direct relation between the geometry of the keyhole and the flow condition at the narrowest position in the channel. It was found that a subcritical flow is clearly present around cylindrical keyholes, while a supercritical flow is present in the region immediately behind the front of U-shaped and wedge-shaped keyholes up to their rear end, where the flow becomes subcritical again. The study suggests that the fast jet resulting from the narrowed flow channel around the keyhole determines the shape and the position of the rear wall of the keyholes at high welding velocities. As a consequence, we have demonstrated that widening the width of the melt pool by means of beam shaping is a useful method to reduce the flow speed in the melt and the Froude number and hence avoid the related undercuts and humping even at high welding speeds.

In summary, the main findings include a novel method for the experimental determination of the velocity of the melt flow flowing around the vapor keyhole during laser welding of metals. It was demonstrated that a supercritical flow influences the rear wall of the keyhole during laser welding at elevated welding speeds. The study revealed that beam shaping is effective in modifying the Froude number of the melt flow around the keyhole. The reduction of the Froude number in the flow obtained with beam shaping effectively prevented the occurrence of undercuts. This knowledge and the new available laser sources that can easily generate different beam shapes allow to specifically influence the Froude number of the melt flow and therefore prevent the occurrence of undercuts. The development of methods to determine the transverse distribution of the melt flow velocities is needed to further investigate the interplay of the melt flow and the shape of the keyhole and will be subject of future research.

Appendix

The following tables list all the used experimental parameters together with other determined parameters which are needed to derive the averaged velocity $\bar{u}(x)$

using Eq. (2) and the Froude numbers using Eqs. (6) or (7). $\bar{u}_{max} = \max(\bar{u}(x))$ stands for the maximum value of the averaged velocity that occurs along the x-direction of the keyholes.

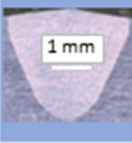
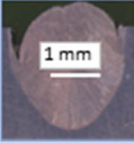


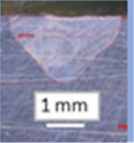
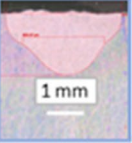
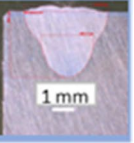
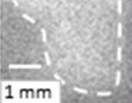

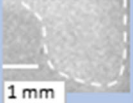
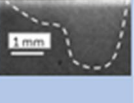

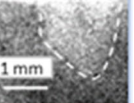
Parameter	Unit	U-Keyhole Fig. 3	Wedge Keyhole Fig. 3	U-Keyhole Fig. 4 & 5	U-Keyhole Fig. 8	U-Keyhole Fig. 4 & 5	U-Keyhole Fig. 4 & 5	Wedge Keyhole Fig. 4 & 5
v	m/s	0,40	0,50	0,50	0,50	0,20	0,13	0,27
P	kW	12	16	16	16	16	11	16
d_f	μm	680	680	680	560	1360	1360	1000
s	mm	1,75	1,4	2,1	2,45	1,8	1,52	2,6
b	mm	1,6	2	1,8	1,8	3	2,8	3,1
A_s	mm^2	2,07	1,78	2,5	3,7	3,7	3,1	5,6
\dot{V}	m^3/s	$828,0 \cdot 10^{-9}$	$890,0 \cdot 10^{-9}$	$1,3 \cdot 10^{-6}$	$1,9 \cdot 10^{-6}$	$740,0 \cdot 10^{-9}$	$413,3 \cdot 10^{-9}$	$1,5 \cdot 10^{-6}$
s_c	mm	1,48	1,3	1,75	2,3	1,6	1,4	2
l_c	m	0,0023	0,0051	0,0027	0,0024	0,004	0,0037	0,0018
y_s	m	0,00027	0,0001	0,00035	0,00015	0,0002	0,00012	0,0006
y_c	m	0,00033	0,00029	0,00038	0,00048	0,00030	0,00027	0,00050
C	mm	3,2	3,6	4	4,2	5,3	4,67	7,86
A_c	mm^2	1,00	0,75	0,98	1,67	2,1	1,82	1,67
A_{ch}	mm^2	1,07	1,03	1,52	2,03	1,60	1,28	3,93
\bar{u}_{max}	m/s	0,37	0,36	0,32	0,41	0,26	0,19	0,11
Fr_s		7,26	11,62	5,50	10,72	5,93	5,53	1,48
Fr_c		6,53	6,87	5,28	5,97	4,82	3,66	1,62
Cross-section								
Key-hole								

Fig. 9 Experimental parameters and determined parameters (Table I)

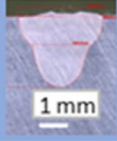
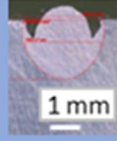
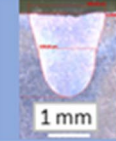
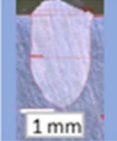
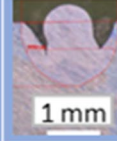
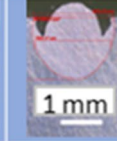
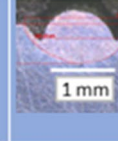
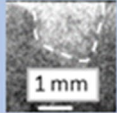

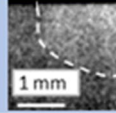
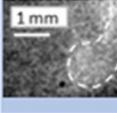

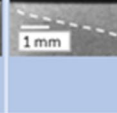

Parameter	Unit	U-Keyhole Fig. 4 & 5	Wedge Keyhole Fig. 4 & 5	U-Keyhole Fig. 4 & 5	Wedge Keyhole Fig. 4 & 5	Cylindrical Keyhole Fig. 4 & 5	Wedge Keyhole Fig. 4 & 5	Wedge Keyhole Fig. 4 & 5
v	m/s	0,30	0,37	0,50	0,13	0,53	0,37	0,67
P	kW	16	16	10	5	14	14	16
d_f	μm	1000	1000	500	500	1000	1000	680
s	mm	2,37	1,5	1,94	2,92	1,24	1,53	0,6
b	mm	2,8	2	1,6	2	1,8	1,9	1,7
A_s	mm^2	4,6	2,6	2,3	4,8	1,8	2,5	0,7
\dot{V}	m^3/s	$1,4 \cdot 10^{-6}$	$953,3\text{E-}9$	$1,2 \cdot 10^{-6}$	$624,0\text{E-}9$	$0,96 \cdot 10^{-6}$	$0,9167 \cdot 10^{-6}$	$0,467 \cdot 10^{-6}$
s_c	mm	2	1,3	1,55	2,5	1,1	1,28	0,48
l_c	m	0,003	0,0022	0,0018	0,00055	0,007	0,0058	0,004
γ_s	m	0,00037	0,0002	0,00039	0,00042	0,00014	0,00025	0,00012
γ_c	m	0,00040	0,00033	0,00030	0,00058	0,00033	0,00023	0,00017
C	mm	6,3	4,6	4,36	6,97	3,62	4,6	2,35
A_c	mm^2	2,1	1,1	0,975	0,735	0,61	1,43	0,31
A_{ch}	mm^2	2,50	1,50	1,33	4,07	1,19	1,07	0,39
\bar{u}_{max}	m/s	0,25	0,27	0,37	0,02	0,27	0,49	0,53
Fr_s		4,18	6,07	5,95	0,37	7,38	9,90	15,44
Fr_c		4,04	4,75	6,74	0,31	4,81	10,26	13,13
Cross-section								
Key-hole								

Fig. 10 Experimental parameters and determined parameters (Table II)

Parameter	Unit	Cylindrical Keyhole Fig. 4 & 5	Cylindrical Keyhole Fig. 4 & 5	Cylindrical Keyhole Fig. 4 & 5	Wedge Keyhole Fig. 4 & 5	Cylindrical Keyhole Fig. 3	Wedge Keyhole Fig. 4 & 5	Wedge Keyhole Fig. 4 & 5
v	m/s	0,33	0,13	0,07	0,60	0,07	0,92	0,50
P	kW	10	1,525	1,65	12,5	3,25	16	16
d_f	μm	500	200	200	630	630	630	630
s	mm	2,9	1,4	1,94	1,4	2,43	1,35	1,5
b	mm	1,6	1,05	1,48	1,44	2,59	1,58	1,89
A_e	mm^2	4,3	1,1	1,98	1,38	4,07	1,49	1,98
\dot{V}	m^3/s	$1,433 \cdot 10^{-6}$	$1,467 \cdot 10^{-7}$	$1,32 \cdot 10^{-7}$	$8,28 \cdot 10^{-7}$	$2,71 \cdot 10^{-7}$	$1,365 \cdot 10^{-6}$	$9,9 \cdot 10^{-7}$
s_c	mm	2,2	1,2	1,75	1,3	2	1,2	1,2
l_c	m	0,0006	0,00022	0,00022	0,0061	0,00067	0,008	0,007
γ_c	m	0,0007	0,0002	0,00019	1E-04	0,00043	0,00015	0,0003
γ_c	m	0,00112	0,00024	0,00035	0,00020	0,00044	0,00022	0,00028
C	mm	3,2	3,45	4,6	3,5	6,2	3,55	4,2
A_c	mm^2	0,72	0,26	0,35	0,68	1,32	0,7	0,8
A_{ch}	mm^2	3,58	0,84	1,63	0,70	2,75	0,79	1,18
\bar{u}_{max}	m/s	0,07	0,04	0,01	0,58	0,03	0,81	0,34
Fr_s		0,81	0,93	0,33	18,61	0,49	21,17	6,25
Fr_c		0,64	0,84	0,24	13,16	0,49	17,38	6,46
Cross-section								
Key-hole								

Fig. 11 Experimental parameters and determined parameters (Table III)

Acknowledgements The research was funded in the framework of the industrial collective research program (IGF no. 20.707N). It was supported by the Federal Ministry for Economic Affairs and Energy (BMWi) through the AiF (German Federation of Industrial Research Associations eV) based on a decision taken by the German Bundestag. The Laser TruDisk8001 (DFG object number: 625617) was funded by the Deutsche Forschungsgemeinschaft (DFG, German Research Foundation) – INST 41/990-1 FUGG. The support of all funders is highly appreciated.

Author contribution All authors contributed to the study conception and design. Material preparation, data collection, and analysis were performed by Eveline N. Reinheimer. The first draft of the manuscript was written by Eveline N. Reinheimer, and all authors commented on previous versions of the manuscript. All authors read and approved the final manuscript.

Funding Open Access funding enabled and organized by Projekt DEAL.

Declarations

Competing interests The authors declare no competing interests.

Open Access This article is licensed under a Creative Commons Attribution 4.0 International License, which permits use, sharing, adaptation, distribution and reproduction in any medium or format, as long as you give appropriate credit to the original author(s) and the source, provide a link to the Creative Commons licence, and indicate if changes were made. The images or other third party material in this article are included in the article's Creative Commons licence, unless indicated otherwise in a credit line to the material. If material is not included in the article's Creative Commons licence and your intended use is not permitted by statutory regulation or exceeds the permitted use, you will need to obtain permission directly from the copyright holder. To view a copy of this licence, visit <http://creativecommons.org/licenses/by/4.0/>.

References

- Reinheimer EN, Fetzter F, Weber R, Graf T (2020) Benefit of high feed rates on the process efficiency in laser beam welding. *Procedia CIRP* 94:718–721
- Fetzter F, Hagenlocher C, Weber R, Graf T (2021) Geometry and stability of the capillary during deep-penetration laser welding of AlMgSi at high feed rates. *Opt Laser Technol* 133:106562. https://puma.uni-stuttgart.de/documents/56e9749c6d9cbd2c573f9230ff98f287/c_hagenlocher/1-s2.0-S0030399220311956-main.pdf. Accessed Jan 2023
- Hagenlocher C, Fetzter F, Weber R, Graf T (2018) Benefits of very high feed rates for laser beam welding of AlMgSi aluminum alloys. *J Laser Appl* 30(1):12015. <https://doi.org/10.2351/1.5003795>
- Dorr N, Dormann L, Klebsch W, Oleniczak A (2021) Logistik, Energie und Mobilität 2030 -Metastudie im BMWi Technologieprogramm IKT für Elektromobilität
- Reinheimer EN, Weber R, Thomas G (2022) Process limit imposed by the occurrence of undercuts during high-speed laser welding. *J Laser Appl* 34.3
- Katayama S (2020) Formation mechanisms and preventive procedures of laser welding defects. In: *Fundamentals and details of laser welding*: Springer, Singapore, p 87–111
- Fabbro R (2010) Melt pool and keyhole behaviour analysis for deep penetration laser welding. *J Phys D: Appl Phys* 43(44):445501. <https://doi.org/10.1088/0022-3727/43/44/445501>
- Bradstreet B (1968) Effect of surface tension and metal flow on weld bead formation. *Weld J* 47(7):314s–322s. <https://ci.nii.ac.jp/naid/10018019783/>. Accessed Jan 2023
- Soderstrom E, Mendez P (2006) Humping mechanisms present in high speed welding. *Sci Technol Weld Join* 11(5):572–579
- Gratzke U, Kapadia PD, Dowden J, Kroos J, Simon G (1992) Theoretical approach to the humping phenomenon in welding processes. *J Phys D Appl Phys* 25(11):1640–1647. <https://doi.org/10.1088/0022-3727/25/11/012/meta>
- Mendez PF, Eagar TW (2003) Penetration and defect formation in high-current arc welding. *Weld J* 82.10:296
- Nguyen TC, Weckman DC, Johnson DA, Kerr HW (2006) High speed fusion weld bead defects. *Sci Technol Weld Join* 11(6):618–633
- Tsukamoto Susumu, Irie Hirosada, Inagaki Michio, Hashimoto Tatsuya (1983) Effect of focal position on humping bead formation in electron beam welding. *Trans National Res Inst Met* 25:62–67. <https://pascal-francis.inist.fr/vibad/index.php?action=getrecorddetail&idt=9461866>. Accessed Jan 2023
- Arata Yoshiaki, Nabegata Eiji (1978) Tandem electron beam welding (report-I). *Trans JWRI* 7:101–109. https://ir.library.osaka-u.ac.jp/repo/ouka/all/6280/jwri07_01_101.pdf. Accessed Jan 2023
- Pirch N, Schmidt H, Oilier B, Kreuz EW, Becker D (1992) Die Humping Instabilität beim Schweißen mit Laserstrahlung. In: *Laser in der Technik/Laser in Engineering*. Springer, Berlin, Heidelberg, p 552–560
- Berger P, Hügel H, Hess A, Weber R, Graf T (2011) Understanding of humping based on conservation of volume flow. *Physics Procedia* 12:232–240
- Berger P, Hügel H (2013) Fluid dynamic effects in keyhole welding – an attempt to characterize different regimes. *Phys Procedia* 41:216–224
- Kinoshita K, Mizutani M, Kawahito Y, Katayama S (2006) Phenomena of welding with high-power fiber laser. *Int Congress Appl Lasers & Electro-Optics* 1:902
- Kouraytem N, Li X, Cunningham R, Zhao C, Parab N, Sun T, Rollett AD, Spear AD, Tan W (2019) Effect of laser-matter interaction on molten pool flow and keyhole dynamics. *Phys Rev Appl* 11:6
- Tenner F, Berg B, Brock C, Klämpfl F, Schmidt M (2015) Experimental approach for quantification of fluid dynamics in laser metal welding. *J Laser Appl* 27(S2):S29003
- Guo Q, Zhao C, Qu M, Xiong L, Hojjatzadeh SMH, Escano LI, Parab ND, Fezzaa K, Sun T, Chen L (2020) In-situ full-field mapping of melt flow dynamics in laser metal additive manufacturing. *Addit Manuf* 31:100939
- Yinglei P, Jiguo S (2020) Understanding humping formation based on keyhole and molten pool behaviour during high speed laser welding of thin sheets. *Eng Res Express* 2(2):25031
- Reinheimer EN, Weber R, Graf T (2022) Influence of the capillary geometry on the weld seam quality during high-speed laser welding. *Procedia CIRP* 111:431–434
- Reinheimer EN, Weber R, Graf T (2022) Process limit imposed by the occurrence of undercuts during high-speed laser welding. *J Laser Appl* 34.3
- Reinheimer EN, Weber R, Thomas G (2022) Influence of high feed rates during laser beam welding on the capillary geometry and the resulting weld seam quality. *High-power laser materials processing: applications, diagnostics, and Systems XI*, vol 11994. SPIE
- ANNO JN (1977) *The mechanics of liquid jets*. Lexington, p 19–46 and p 61–66
- Albright CE, Chiang S (1988) High speed laser welding discontinuities. *Int Congress Appl Lasers & Electro-Optics* 1988(1). Laser Institute of America
- Shimada W, Hoshinouchi S (1983) A study on bead formation by low pressure TIG arc and prevention of under-cut bead. *Trans Jpn Welding Soc* 14(1):60–61. <https://cir.nii.ac.jp/crid/1541417145288196736>. Accessed Jan 2023
- Nguyen TC, Weckman DC, Johnson DA, Kerr HW (2005) The humping phenomenon during high speed gas metal arc welding. *Sci Technol Weld Join* 10(4):447–459
- Pandey BR (2016) Open channel surges. *J Adv Coll Engin Mgt* 1:35. <https://www.nepjol.info/index.php/jacem/article/view/14919>. Accessed Jan 2023
- Rapp BE (2022) *Microfluidics: modeling, mechanics and mathematics*. 2nd edn. San Diego: Elsevier, (Micro and Nano Technologies Ser)
- Gyasi EA (2018) On adaptive intelligent welding: technique feasibility in weld quality assurance for advanced steels
- Kumar A, Zhang W, Kim CH, Debroy T (2005) A smart bi-directional model of heat transfer and free surface flow in gas-metal-arc fillet welding for practising engineers. *Weld World* 49(9–10):32–48. <https://doi.org/10.1007/bf03266488>
- Kumar A, Debroy T (2007) Heat transfer and fluid flow during gas-metal-arc fillet welding for various joint configurations and welding positions. *Metall Mater Trans A* 38(3):506–519. <https://doi.org/10.1007/s11661-006-9083-4>
- Hager WP (1992) *Energy dissipators and hydraulic jump*. Springer, Netherlands Water Science and Technology Library v.8, Dordrecht
- Uddin MN (1995) *High speed laser welding instability and optimization*. University of Windsor, Canada
- Harooni M, Carlson B, Kovacevic R (2014) Dual-beam laser welding of AZ31B magnesium alloy in zero-gap lap joint configuration. *Opt Laser Technol* 56:247–255
- Simonds BJ, Tanner J, Artusio-Glimpse A, Williams PA, Parab N, Zhao C, Sun T (2022) Asynchronous AM bench 2022 challenge data: real-time, simultaneous absorptance and high-speed xray imaging
- French RH (1985) *Open-channel hydraulics*

40. Abt F, Boley M, Weber R (2011) Graf T (2018) X-ray videography for investigation of capillary and melt pool dynamics in different materials. *Int Congress Appl Lasers & Electro-Optics* 1:179–186
41. Fetzer F, Boley M, Weber R, Graf T (2017) Comprehensive analysis of the capillary depth in deep penetration laser welding. In: Kaielerle S, Heinemann SW (eds) *High-power laser materials processing: applications, diagnostics, and systems VI*, vol 10097. SPIE, pp 73–80
42. Lind J et al (2021) Influence of the laser cutting front geometry on the striation formation analysed with high speed synchrotron X-ray imaging. *IOP Conf Ser Mater Sci Eng* 1135(1)
43. Boley M, Fetzer F, Weber R, Graf T (2019) High-speed x-ray imaging system for the investigation of laser welding processes. *J Laser Appl* 31(4):42004
44. Fetzer F, Hagenlocher C, Weber R, Graf T (2021) Geometry and stability of the capillary during deep-penetration laser welding of AlMgSi at high feed rates. *Opt Laser Technol* 133:106562
45. Hgel H, Graf T (2023) *Materialbearbeitung mit Laser*. Springer Fachmedien, Wiesbaden, Wiesbaden
46. Neumann S (2012) Einflussanalyse beim single mode faserlaser-schweien zur vermeidung des humping-phnomens. Bias Verlag
47. Hansen KS, Kristiansen M, Olsen FO (2014) Beam shaping to control of weldpool size in width and depth. *Physics Procedia* 56:467–476
48. Patschger A (2016) *Grundlegende Untersuchungen zum Prozessverstndnis des Laserstrahl-Mikroschweiens von metallischen Folien*. Universittsbibliothek Ilmenau, Ilmenau
49. Huang L, Liu P, Zhu S, Hua X, Dong S (2020) Experimental research on formation mechanism of porosity in magnetic field assisted laser welding of steel. *J Manuf Process* 50:596–602

Publisher's Note Springer Nature remains neutral with regard to jurisdictional claims in published maps and institutional affiliations.